 CMES, vol.74, no.3, pp.203-232, 2011

Large Eddy Simulation of Turbulent-Supersonic Boundary Layer Subjected to Multiple Distortions

W. A. El-Askary[1]

Abstract: Large eddy simulation (LES) is a viable and powerful tool to analyze unsteady three- dimensional turbulent flows. In this paper, the method of LES is used to compute a plane turbulent supersonic boundary layer subjected to different pressure gradients. The pressure gradients are generated by allowing the flow to pass in the vicinity of an expansion-compression ramp (inclined backward-facing step with leeward-face angle of 25 degrees) for an upstream Mach number of 2.9. The inflow boundary condition is the main problem for all turbulent wall-bounded flows. An approach to solve this problem is to extract instantaneous velocities, temperature and density data from an auxiliary simulation (inflow generator). To generate an appropriate realistic inflow condition to the inflow generator itself the rescaling technique for compressible flows is introduced. In this method Morkovin's hypothesis in which the total temperature fluctuations are neglected compared with the static temperature fluctuations is applied to rescale and generate the temperature profile at inlet. This technique was successfully developed and applied by the present author for a large eddy simulation of subsonic three-dimensional boundary layer of a smooth curved ramp.
The present LES results are compared with the available experimental as well as numerical data. The positive impact of LES is proven by the convincing agreement of the obtained results with the experimental data compared with published numerical work and sheds the light on the quality of the compressible inflow generator method.

Keywords: Large eddy simulation; shock wave boundary layer interaction; pressure gradient; inflow boundary condition.

[1] Mechanical Power Engineering Department, Faculty of Engineering, Menoufiya University, Shebin El-Kom, Egypt. Corresponding author, Tel.: +2-0105255817, +2-048-3486965; Fax: +2-048-2235695. *Email address*: wageeh_elaskary@yahoo.com

Nomenclature

a	Speed of sound
$c_{p/v}$	Specific heat at constant pressure/volume
C_p	Wall-pressure coefficient
C_f	Skin-friction coefficient
e	Total energy per unit mass
F_α	Flux vector
J	Coordinate-transformation Jacobian
k	Turbulent kinetic energy
L_d	Horizontal length including ramp and its downstream
L_u	Upstream length before the ramp onset
M_∞	Free-stream Mach number
M_l	Local Mach number
M_t	Turbulent Mach number
n	Normal vector
p	Pressure
Q	Vector of the conservative variables
R	The gas constant
R_{ij}	Two-point velocity correlation
Re	REYNOLDS number
r	Recovery factor
S	Source term in sponge layer
t	Time
T	Static temperature
T_o	Stagnation temperature
U	Local streamwise-mean velocity
U^c, V^c, W^c	Contravariant velocity components
U_{vd}	van-Driest transformed mean velocity
U^+	Non-dimensional velocity, $U^+ = U/u_\tau$
U_∞	Free-stream velocity
u, v, w	Unsteady velocity components in a Cartesian system
$u'u', v'v', u'v'$	Streamwise, normal and shear Reynolds stresses, respectively
u_τ	Friction velocity, $u_\tau = \sqrt{\tau_w/\rho_w}$
x, y, z	Cartesian coordinates in streamwise, transverse and spanwise direction
y^+	Non-dimensional inner coordinate of boundary layer, $y^+ = u_\tau y/\nu$
y	Distance from the wall

Greek symbols

α	Coefficients of Runge-Kutta
β	Ramp angle
β_s	Rescaling factor
γ	Ratio of specific heats,$\gamma = c_p/c_v$
Δx^+	Non-dimensional grid spacing in wall coordinate
Δy^+	Boundary layer thickness
Δz^+	Inflow boundary layer thickness
δ_1	Displacement thickness
δ_{ij}	Kronecker delta (δ_{ij} = 1 if $i = j$, and δ_{ij}= 0 otherwise)
κ	Von Karman constant $\kappa = 0.41$
λ	Coefficient of thermal conductivity
μ	Dynamic viscosity
ν	Kinematic viscosity, $\nu = \mu/\rho$
ξ, η, ζ	General curvilinear coordinates
ρ	Fluid density
σ_{ij}	Viscous stress tensor
$\sigma_{\max}$	Maximum damping factor in sponge layer
σ_s	Damping factor in sponge layer
σ_w	(Time averaged) wall shear stress
θ	Momentum thickness
$\Phi(\vec{\xi}, t)$	Flow variable to be filtered by LES
$\bar{\Phi}(\vec{\xi}, t)$	Filtered (large scale) component
$\tilde{\Phi}(\vec{\xi}, t)$	Favre-averaged component
$\Phi'_{SGS}(\vec{\xi}, t)$	Unfiltered (subgrid-scale) component
Θ_i	Subgrid scale heat flux
Υ_j	Subgrid scale energy flux
Ξ_i	Subgrid scale work done

Calligraphic symbols

i, j, k	Component i, j, k of a vector
in	Inflow to the test case
re	Rescaling section
ref	Reference value
x, y, z	Partial derivative with respect to x, y, z
w	Wall condition
∞	Free-stream value

Acronyms

AUSM	Advective Upstream Splitting Method
DNS	Direct Numerical Simulation
LES	Large-Eddy Simulation
MILES	Monotone Integrated Large Eddy Simulation
SGS	Subgrid Scale
SWTBLI	Shock Wave/Turbulent Boundary Layer Interaction

1 Introduction

The Shock Wave/Turbulent Boundary Layer Interaction (SWTBLI) is a common phenomenon in high-speed flight and still an important problem for supersonic aircraft designers. Such phenomenon plays an important role both for internal and external aerodynamic. This interaction can lead to an increase of drag, separation, and performance loss. The studies presented by Knight and Degrez(1998) introduced the capability of Reynolds-Averaged Navier-Stokes (RANS) method for prediction of 2-D and 3-D shock wave turbulent boundary layer interactions. All studies concluded that conventional RANS methods accurately predicted the mean surface pressure and not capable to predict the separation location. Recently, large eddy simulation (LES) and direct numerical simulation (DNS) have been applied to the problem of SWTBLI with significant success; see Adams (1997), Urbin, Knight and Zheltovodov(2000), Rizzetta, Visbal and Gaitonde(2001) and El-Askary , Schröder and Meinke(2003). As explained in the work of Knight, Yan, Panaras and Zheltovodov(2003) that the first systematic combined experimental and numerical study of an expansion-compression corner by Zheltovodov, Schuelein and Horstman(1993) showed that several different turbulence models did not accurately predict the separation and attachment positions. Their turbulence models failed in capturing the skin friction coefficient distribution. Knight, Yan, Panaras and Zheltovodov(2003) tried with LES without rescaling the temperature fluctuation at the inflow and indictable disagreements with the experimental data were obtained. Inflow boundary conditions for hybrid LES/RANS approaches were developed by Xiao, Edwards and Hassan(2003). They are based on an extension of the rescaling-reintroducing method developed for LES to a hybrid scheme. A rescaling of the velocity and temperature fluctuations was provided with the introduction of fixed mean profiles at the inflow. An assumption without any proof was also introduced in which the turbulent fluctuations of the temperature in the outer layer have the same rescaling factor of the inner layer. The approach was tested for a flat plate and then applied to the study of a 25-deg compression-expansion corner for a Mach

number of 2.9. Significant differences with the experimental data opened the way to modify either the hybrid approach or the inflow boundary condition. A rescaling method based on Morkovin's hypothesis and generalized temperature-velocity relationships was introduced by Xu and Martin(2004) to simulate a compressible turbulent boundary layer. The results showed good agreement with only theoretical work.

Extending the method of Lund, Wu and Squires(1998) to compressible flows showed good results in the presence of other simulations and experimental works, see El-Askary, Meinke and Schröder(2001) and El-Askary(2009). The efficient performance of the method given in El-Askary, Meinke and Schröder(2001) and El-Askary(2009) was also noticed in the work of Schröder, Meinke, Ewert and El-Askary(2001) and Sagaut, Garnier, Tromeur, Larcheveque and Labourasse(2004). Comparing the results of LES from previous researches in the field of SWTBLI, it is noticed that the method of El-Askary(2003) generates an efficient realistic inflow condition to supersonic boundary layer in a simple way, see Zheltovodov(2006).

The objective of the present work is to assess the capability of LES methodology with an efficient extended compressible inflow technique in the presence of a changed sequence of interactions. In this sequence, the boundary layer interacts first with expansion fan and then with shock wave. The computation method used here is the compressible LES. The Monotone Integrated LES (MILES) approach, described by Boris, Grinstein, Oran and Kolbe(1992), is used. This concept, which is based on monotone schemes, has been proven extremely successful on structured and unstructured grids. Due to the special treatment of the small structures LES unlike DNS can be applied to more complex flows and flows at larger Reynolds number, such as ramp and axpansion-compression corner flows [Knight, Yan, Panaras and Zheltovodov(2003)], since an LES requires much less computational effort.

2 Governing equations

The governing equations are the unsteady three-dimensional compressible Navier-Stokes equations, written in generalized curvilinear coordinates (ξ, η, ζ) as:

$$\frac{\partial Q}{\partial t} + \frac{\partial (Fc_i - Fv_i)}{\partial \xi_i} = 0, \tag{1}$$

In large eddy simulation, the large-scale field is computed directly from the solution of the local volume-averaged Navier-Stokes equations, and the small-scale stresses are modeled. The subgrid scale model then represents the effects of the small scales on the large-scale motions. The decomposition of any variable $\Phi(\vec{\xi}, t)$ can be rep-

resented as a large-scale $\bar{\Phi}(\vec{\xi},t)$ plus a small scale or subgrid-scale $\Phi'_{sgs}(\vec{\xi},t)$ part:

$$\Phi(\vec{\xi},t) = \bar{\Phi}(\vec{\xi},t) + \Phi'_{sgs}(\vec{\xi},t) \tag{2}$$

In compressible flows also temperature and density fluctuations must be considered. The problem of establishing the appropriate form of the averaged equations of a compressible fluid can be simplified by using the density-weighted averaging procedure suggested by Favre(1965)

$$\tilde{\Phi}(\xi,\eta,\zeta,t) = \frac{\overline{\rho(\xi,\eta,\zeta)\Phi(\xi,\eta,\zeta,t)}}{\overline{\rho(\xi,\eta,\zeta)}} \tag{3}$$

Thus, a variable $\Phi(\xi,\eta,\zeta,t)$ is decomposed into its Favre-filtered component $\tilde{\Phi}(\xi,\eta,\zeta,t)$ and a fluctuating component $\Phi''(\xi,\eta,\zeta,t)$.

With this formulation and the metric Jacobian J, the vector of dependent variables $\tilde{Q}$ and the vector fluxes $\tilde{F}$ are given by:

$$\tilde{Q} = \frac{1}{J}\begin{pmatrix} \bar{\rho} \\ \bar{\rho}\tilde{u} \\ \bar{\rho}\tilde{v} \\ \bar{\rho}\tilde{w} \\ \bar{\rho}\tilde{e} \end{pmatrix} \tag{4}$$

$$\tilde{F}c_i = \frac{1}{J}\begin{pmatrix} \bar{\rho}\tilde{U}_i^c \\ \bar{\rho}\tilde{U}_i^c\tilde{u} + \frac{\partial\xi_i}{\partial x}\bar{p} \\ \bar{\rho}\tilde{U}_i^c\tilde{v} + \frac{\partial\xi_i}{\partial y}\bar{p} \\ \bar{\rho}\tilde{U}_i^c\tilde{w} + \frac{\partial\xi_i}{\partial z}\bar{p} \\ \bar{\rho}\tilde{U}_i^c\tilde{e} + \tilde{U}_i^c\bar{p} \end{pmatrix} \tag{5}$$

and

$$\tilde{F}v_i = \frac{1}{J}\begin{pmatrix} 0 \\ \frac{\partial\xi_i}{\partial x_j}\tilde{\sigma}_{j1} + \tau_{j1} \\ \frac{\partial\xi_i}{\partial x_j}\tilde{\sigma}_{j2} + \tau_{j2} \\ \frac{\partial\xi_i}{\partial x_j}\tilde{\sigma}_{j3} + \tau_{j3} \\ \frac{\partial\xi_i}{\partial x_j}\tilde{b}_j + \Upsilon_j \end{pmatrix} \tag{6}$$

J is identified as the Jacobian determinant and denoted by $J = |\frac{\partial(\xi,\eta,\zeta)}{\partial(x,y,z)}|$.

The contravariant velocity in the i direction is given by:

$$\tilde{U}_i^c = \frac{\partial \xi_i}{\partial x}\tilde{u} + \frac{\partial \xi_i}{\partial y}\tilde{v} + \frac{\partial \xi_i}{\partial z}\tilde{w} \tag{7}$$

where, ξ_i reads ξ, η, and ζin streamwise, normal, and spanwise direction, respectively.

The stress terms σ_{ij} are also transformed in terms of the ξ, η, and ζ derivatives, in which

$$\tilde{\sigma}_{ij} = \mu(\tilde{T})\left(\frac{\partial \tilde{u}_i}{\partial \xi_k}\frac{\partial \xi_k}{\partial x_j} + \frac{\partial \tilde{u}_j}{\partial \xi_k}\frac{\partial \xi_k}{\partial x_i} - \frac{2}{3}\delta_{ij}\frac{\partial \tilde{u}_k}{\partial \xi_l}\frac{\partial \xi_l}{\partial x_k}\right), \tag{8}$$

where $\mu(\tilde{T})$ is the molecular viscosity based on the Favre-filtered static temperature $\tilde{T}$ using the exponential law $\frac{\mu}{\mu_{ref}} = \left(\frac{\tilde{T}}{\tilde{T}_{ref}}\right)^{0.72}$, where the subscript ref denotes a reference value. All reference values considered in the present work are taken at a stagnation condition. The quantities $\tilde{b}_j$ can be written as:

$$\tilde{b}_j = \tilde{u}_i\tilde{\sigma}_{ji} + \lambda(\tilde{T})\left(\frac{\partial \tilde{T}}{\partial \xi}\frac{\partial \xi}{\partial x_j} + \frac{\partial \tilde{T}}{\partial \eta}\frac{\partial \eta}{\partial x_j} + \frac{\partial \tilde{T}}{\partial \zeta}\frac{\partial \zeta}{\partial x_j}\right) \tag{9}$$

in which the subgrid viscous diffusion work $(\overline{u_i\sigma_{ji}} - \tilde{u}_i\tilde{\sigma}_{ji})$ is neglected as in Knight, Zhou, Okong'o and Shukla(1998). Every subscript i, j and k takes on values 1, 2 or 3 to represent variables in ξ, η and ζ directions (for example U^c, V^c andW^c), respectively. The pressure can be obtained via the equation of state for a perfect gas and the total energy relation

$$\bar{p} = (\gamma - 1)\left[\bar{\rho}\tilde{e} - \frac{\bar{\rho}}{2}\tilde{u}_i^2 - \bar{\rho}k_{sgs}\right] \quad , \tag{10}$$

where $\bar{\rho}k_{sgs}$g is the subgrid-scale kinetic energy per unit volume represented by the following relation

$$\bar{\rho}k_{sgs} = \frac{1}{2}\bar{\rho}(\overset{\sim}{u_i^2} - \tilde{u}_i^2) \tag{11}$$

and $\gamma = \frac{c_p}{c_v}$ is the ratio of specific heats. The specific heats at constant pressure c_p and constant volume c_v are constant for a perfect gas and can be calculated from $c_v = R/(\gamma - 1)$with $\gamma = 1.4$ and R is the gas constant (R = 287J/kgK for air). The subgrid-scale stresses (SGS) $\tau_{ij} = \bar{\rho}(\overset{\sim}{U_i^c u_j} - \tilde{U}_i^c\tilde{u}_j)$ and the subgrid-scale energy

term $\Upsilon_i = \bar{\rho}(\widetilde{eU_i^c} - \tilde{e}\tilde{U}_i^c) + (\widetilde{pU_i^c} - \tilde{p}\tilde{U}_i^c)$ can be calculated via a suitable subgrid-scale model. The subgrid-scale term $\Upsilon_i$gcan be divided into a subgrid scale heat flux Θ_i and a subgrid work done by subgrid scales Ξ_i.

$$\Upsilon_i = \Theta_i + \Xi_i \tag{12}$$

where,

$$\Theta_i = c_p\bar{\rho} \overbrace{(\widetilde{U_i^c T} - \tilde{U}_i^c\tilde{T})}^{\text{subgrid temperature flux}} \tag{13}$$

and

$$\Xi_i = \frac{1}{2}\bar{\rho}\left(\overbrace{(\widetilde{u_k^2 U_i^c} - \tilde{u}_k\tilde{u}_k\tilde{U}_i^c)}^{\text{triple correlation}} - 2k_{sgs}\tilde{U}_i^c\right) \tag{14}$$

in which $\overline{\rho U_i^c e} = \bar{\rho}\,\widetilde{U_i^c e} = \bar{\rho}c_v\widetilde{U_i^c T} + \frac{1}{2}\bar{\rho}\,\widetilde{U_i^c u_k^2}$ and $\widetilde{U_i^c p} = \bar{\rho}R\widetilde{U_i^c T}$ have been substituted. The term Ξ_i can be further simplified to yield [Knight, Zhou, Okong'o and Shukla(1998)]:

$$\Xi_i \approx \frac{1}{2}\tau_{ki}\tilde{u}_k \tag{15}$$

The present large-eddy simulation is carried out using the MILES technique [Boris, Grinstein, Oran and Kolbe(1992)] to represent the effect of non-resolved subgrid scales. MILES is designed from first principles to provide an accurate and efficient computational model by applying numerical methods optimized for flows with weak discontinuities. In this view, the numerical algorithm defines the entire energy transfer between resolved and subgrid scales. This requires a high-order accurate numerical algorithm, which minimizes numerical dissipation, e.g., an AUSM algorithm and no explicit subgrid-scale model is employed, i.e., $\tau_{ij} = 0$, $\Theta_i = 0$, $k_{sgs} = 0$, and $\Xi_i = 0$. MILES is explained extensively in Boris, Grinstein, Oran and Kolbe(1992) and Fureby and Grinstein(2002) where many tests were carried out and it was also used by Yan, Urbin, Knight and Zheltovodov(2000) to simulate different compression-corner flows at Mach number $M_\infty = 2.9$ on unstructured grids. However, in MILES approach, the intrinsic dissipation of the numerical scheme is assumed to transfer the energy from the large to the small scales. In the following discussions the tilde and the overbar are dropped for simplification.

3 Numerical method

For the numerical representation of the conservation laws in their integral form, they will have to be accurately represented in a finite number of discrete cells. The computational domain is subdivided into a finite number of non-overlapping control volumes to generate a structured mesh over which the variables are calculated at the centroid of each control volume in the mesh. Interpolation is used to express the values of the variables at the control volume surfaces in terms of centroid values. In the following two subsections, the algorithm to numerically integrate the governing equations in space and then, the time integration will be shortly presented.

3.1 Spatial integration

The discretization of the governing equations is based on a mixed central-upwind AUSM (advective upstream splitting method) scheme using a centered 5-point low dissipation stencil to compute the pressure derivative in the convective fluxes. The large-eddy simulations are carried out using the MILES technique as reported by Renze, Schröder and Meinke(2008) and Grinstein and Fureby(2002) to represent the effect of the non-resolved subgrid scales. As a consequence, the intrinsic dissipation of the numerical scheme is assumed to transfer energy from the large to the small scales. Thus, it serves as a minimal implicit SGS model. An extensive study of the AUSM algorithm with different SGS models and its dependence on the grid solution has been reported by Meinke, Schröder and Krause(2002). A more detailed discussion of the application of the MILES technique is given in El-Askary, Meinke and Schröder(2001) and El-Askary, Schröder and Meinke(2003).

The discretization of the convective fluxes Fc_i in the governing equations is a second-order accurate AUSM formulation. In the AUSM scheme the convective and pressure terms within the inviscid flux vectors are treated separately. The convective terms are approximated upstream biased using a properly defined cell interface velocity, while the pressure term is computed using the sound velocity. The viscous fluxes Fv_i are discretized using central differences of second-order accuracy.

3.2 Time integration

The discretized system of equations states an initial value problem in the time direction. With a solution at time-level n a successive solution at the following time-level n+1 can be calculated. In the present study the frequently applied Runge-Kutta method is used. For the time integration the conservation equations are written as:

$$\frac{\partial Q}{\partial t} \approx \frac{Q^{n+1} - Q^n}{\Delta t} = RHS(Q^n) \tag{16}$$

where n is the time level and Δt is the time step. In order to determine the right-hand side ($RHS(Q^n)$), the space discretization of all fluxes must be carried out as previously discussed. The basic idea of the Runge-Kutta method is to evaluate the right-hand side of the differential equation 16 at several numerical values of Q in the interval between $n\Delta t$ and $(n+1)\Delta t$ and to combine them to obtain an efficient high-order approximation of Q^{n+1}. All computations in the present research are performed with an explicit 5-step Runge-Kutta time stepping scheme of second-order accuracy is used for the temporal integration. The coefficients in the Runge-Kutta steps are chosen to be α = (6/24, 4/24, 9/24, 12/24, 24/24). They are optimized for maximum stability of a central scheme.

4 Boundary conditions

There are two geometries to be simultaneously simulated, a supersonic flat plate boundary layer at freestream Mach number $M_\infty = 2.9$ (Inflow Generator) and the expansion-compression ramp (inclined backward-facing step) of 25 degrees at the same Mach number. The boundary conditions for the flat plate and the expansion-compression ramp flows read as follows. On all solid surfaces the no-slip condition and an adiabatic wall, i.e., $u_i = 0$ and $\partial T/\partial n = 0$, where n is the direction normal to the wall, are imposed. Periodic boundary conditions are applied in the homogeneous spanwise direction of thickness $1.36\delta_o$. This sufficient spanwise extension was tested and satisfied in El-Askary, Schröder and Meinke(2003), Guo, Schröder and Meinke(2006) and El-Askary(2009).

At supersonic outflow all variables can be extracted from the first inner point of the solution domain as long as the local Mach number is greater than unity. For boundary points where the local streamwise Mach number is subsonic, the extrapolation process is implemented for all variables except the pressure. The pressure is set equal to the pressure at the grid point at which the Mach number first becomes supersonic. At subsonic upper boundary of the inflow generator, non-reflecting boundary condition with pressure relaxation are applied [Poinsot and Lele(1992)], which are completed by a sponge layer in which the source terms S in sponge layer are computed as a function of the deviation of the instantaneous conservative variables $Q(\vec{x},t)$ from the analytical solution Q_∞ which is based on free-stream values $S = \sigma_s\left(Q(\vec{x},t) - Q_\infty\right)$. The parameter σ_sg is computed as a function of the distance from the boundaries and increases from zero to $\sigma_{\max}$ within the sponge layer zone. The value of $\sigma_{\max}$ was chosen to be 0.5, which has been determined in test simulations under the condition to minimize numerical reflections, see El-Askary, Schröder and Meinke(2003). At the upper boundary of the expansion-compression ramp, simple-wave condition is specified, see Roache(1976).

In most applications, the state of the inflow turbulence can have a substantial in-

fluence on the results of unsteady simulations. Particular attention must be paid to this issue and was considered with success in many tests, see El-Askary(2003) and El-Askary(2009). For the expansion-compression ramp flow the instantaneous velocity and temperature distributions for the inflow boundary are generated via simultaneous simulation of turbulent flat plate boundary layer (Inflow Generator). This boundary layer simulation also requires an inlet boundary condition, which can be derived by a compressible extension of the method of Lund, Wu and Squires(1998). The turbulent inflow boundary conditions in spatially developing compressible flows are quite important, since in most cases the influence of the upstream conditions persists for large distances downstream. A simple method is the use of periodic boundary conditions, which is unfortunately restricted to a few geometries like the channel flow. Spalart(1988) was able to extend the area of application to an incompressible turbulent boundary layer by using coordinate transformations. However, Spalart's approach is restricted to flows whose mean streamwise variation is small compared to the transverse variation. A further disadvantage is the complexity of the method. Therefore, Lund et al. [10] extended Spalart's idea. An auxiliary simulation, which produces its own inflow conditions by rescaling the velocity field from a downstream location and reintroducing it at the inflow, was used to extract instantaneous planes of velocity. Therefore, they were denoted semi-periodic boundary conditions combined with a separate simulation.

To be able to account for Mach number and temperature effects across the boundary layer, El-Askary et al. [5] and El-Askary [12] extended the rescaling method of Lund, Wu and Squires(998). The present rescaling-recycling method is based on Morkovin's hypothesis; see Bradshaw(1977), in which the temperature fluctuation T' can be calculated assuming a negligible total temperature fluctuation T_t' compared with the static temperature fluctuation. This assumption is valid in the present work since the flow under consideration is supersonic flow at $M_\infty = 2.9$. Following Bradshaw(1977) the static temperature fluctuation is introduced

$$\frac{T'(y,z,t)}{T(y,z,t)} = -(\gamma-1)M_l^2 \frac{u'(y,z,t)}{u(y,z,t)}, \tag{17}$$

where M_l is the local Mach number. For the mean static temperature T, Walz's equation(1969) is locally applied as:

$$\frac{T}{T_\infty} = 1 + \frac{(\gamma-1)}{2} r M_\infty^2 \left(1 - \frac{U^2}{U_\infty^2}\right), \tag{18}$$

where r is the recovery factor and M_∞ is the free-stream Mach number. The implementation of the method was recently provided by El-Askary(2009) and also

tested in film cooling flow simulation by Guo, Schröder and Meinke(2006) with good findings, so it will be used in the present work.

However, a method without any rescaling of temperature was developed by Urbin and Knight(2001) and used also in Knight, Yan, Panaras and Zheltovodov(2003), which may affect their LES results as shown later. Unlike Lund, Wu and Squires(1998) who used the momentum thickness, the displacement thickness is incorporated in the rescaling formulation to reduce the nonlinearity effects of the momentum thickness. The displacement thickness is a linear integration function of the velocity whereas that of the momentum thickness is a quadratic function. The latter accumulates more inaccuracies from the spanwise spatial average such that a slightly less benign behavior at the boundaries results. The code of this developed inflow boundary condition was validated for a variety of turbulent subsonic and supersonic flows by comparing the results with that obtained from experiments and other computations, see El-Askary, Schröder and Meinke(2003) and Schröder, Meinke, Ewert and El-Askary(2001) and El-Askary(2009).

5 Results and discussion

The computation performed here is corresponding to the physical experiments of Zheltovodov, Trofimov, Filippova and Yakovlev(1990) and Zheltovodov, Trofimov, Schuelein and Yakovlev(1990) as presented with simulation by Knight, Yan, Panaras and Zheltovodov(2003), which contains all necessary results for comparison. The flow parameters considered are inflow freestream Mach number $M_\infty = 2.9$ and Reynolds number $Re_{\delta_o} = U_\infty \delta_o / \nu_\infty = 2 \times 10^4$, where δ_o is thickness of the boundary layer at the inlet to the considered domain. In order to reduce the computation costs and verify the quality of the present LES results in view of that previously performed by Knight, Yan, Panaras and Zheltovodov(2003), the present simulation is carried out only at the same Reynolds number considered in Knight, Yan, Panaras and Zheltovodov(2003). This equilibrium turbulent supersonic boundary layer expands over an angle $\beta = 25$ inclined backward-facing step, see Fig. 1. The distance along the inclined surface is $7.1\delta_o$ (i.e., the horizontal distance between the expansion and compression corner points is $6.43\delta_o$ and the vertical distance between the two horizontal surfaces is $3\delta_o$). The origin of the coordinates begins at the inflow to the inclined backward-facing step geometry in which x, y and z are aligned in the streamwise, transverse and spanwise directions, respectively. The inclined face starts at a distance of $L_u = 4\delta_o$ from the inflow boundary of the computational domain and followed by a flat surface of length $13.57\delta_o$, i.e., $L_d = 20\delta_o$. The inflow height is $3.4\delta_o$ and the spanwise extension is $1.36\delta_o$; the same of the inflow generator.

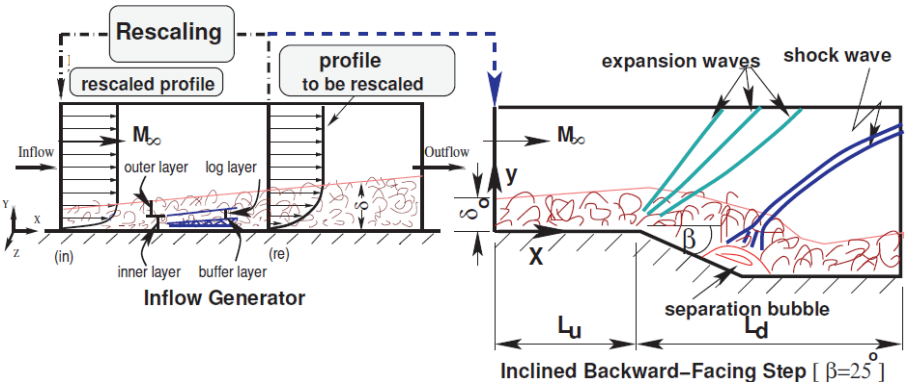

Figure 1: Schematic representation of rescaling process to inflow generator and extraction of inflow boundary condition to expansion-compression ramp (inclined backward-facing step).

5.1 Undisturbed turbulent boundary layer (inflow generator) results

The inflow turbulent boundary condition is obtained from simultaneous simulation of flat plate supersonic boundary layer (inflow generator) of $433\times113\times33$ grid points. The computational domain of the flat plate is $L_x = 18\delta_o$, $L_y = 3.4\delta_o$ and $L_z = 1.36\delta_o$. Adams(2000) chose a spanwise extent of $1.2185\delta_o$ for DNS of 18-degrees compression ramp and found that it was sufficient to enforce a periodic boundary condition in the spanwise direction. Xu and Martin(2004) used $1.43\delta_o$g and $1.5\delta_o$ in DNS of supersonic boundary layer with good results. The spanwise width L_z chosen here is however based on the two-point correlation of the velocity components in spanwise direction, which will be sufficiently small ($O(0.1)$) at the tail end of the correlation curve. The interested correlation to be visualized in streamwise and spanwise directions is that of the streamwise u' and spanwise w' velocity fluctuations. It is defined as:

$$R\left(u'(r)u'(r+\Delta r)\right) = \frac{\overline{u'(r,t)u'(r_+\Delta r,t)}}{\sqrt{\overline{u'^2(r,t)}}\sqrt{\overline{u'^2(r+\Delta r,t)}}},$$

where the reference point is taken to be at $r(x_{ref}, y_{ref}, z_{ref})$ and Δr is the separation distance between the two correlated points. Iso-correlation contour maps are a useful means of presenting the broadband correlation. These maps are comprised of lines of constant correlation values and provide a picture of the overall shape and extent of the average large scale structure of the flow. The two-point correlation contours are computed at several distances traversing vertically across the boundary

layer.

Figures 2 and 3 show the streamwise-component $R(u'(r)u'(r+\Delta r))$ and spanwise-component $R(w'(r)w'(r+\Delta r))$ correlations in horizontal planes parallel to the plate surface and evaluated at non-dimensional wall distances, y^+ =37.5, 125, 200 and 250. These are corresponding to outer values (y/δ_o) of 0.15, 0.5, 0.8 and 1.0, respectively. The results show that the fluctuating velocity in the outer layer is correlated over larger distances than that near the wall. Nearer to the wall the structures evidence that the eddy scales are smaller than that near the edge of the boundary layer. This means that the main eddies of the flow have diameters proportional to the distance of their centers from the wall, because the motion is directly influenced by its presence.

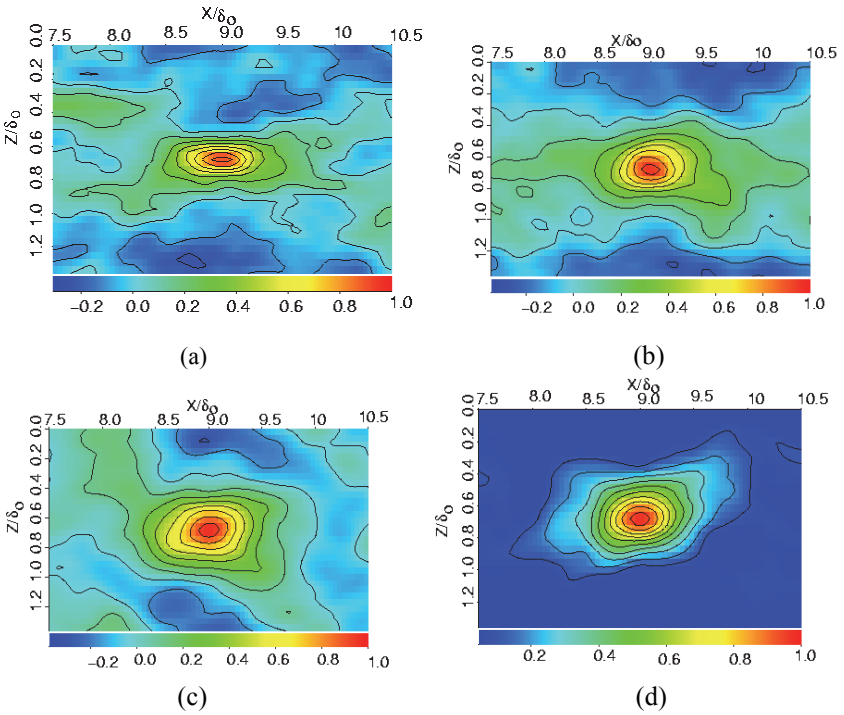

Figure 2: Streamwise correlation contours $R(u'(r)u'(r+\Delta r))$ in $z-x$ plane at different vertical positions y/δ

The streamwise, spanwise and vertical components of the correlation coefficient profiles at vertical distances of y/δ_o=0.05, 0.15, 0.5, 0.8 and 1.0 are presented in Fig. 4. In all plots z_{ref} is taken to be at the middle of spanwise direction. The

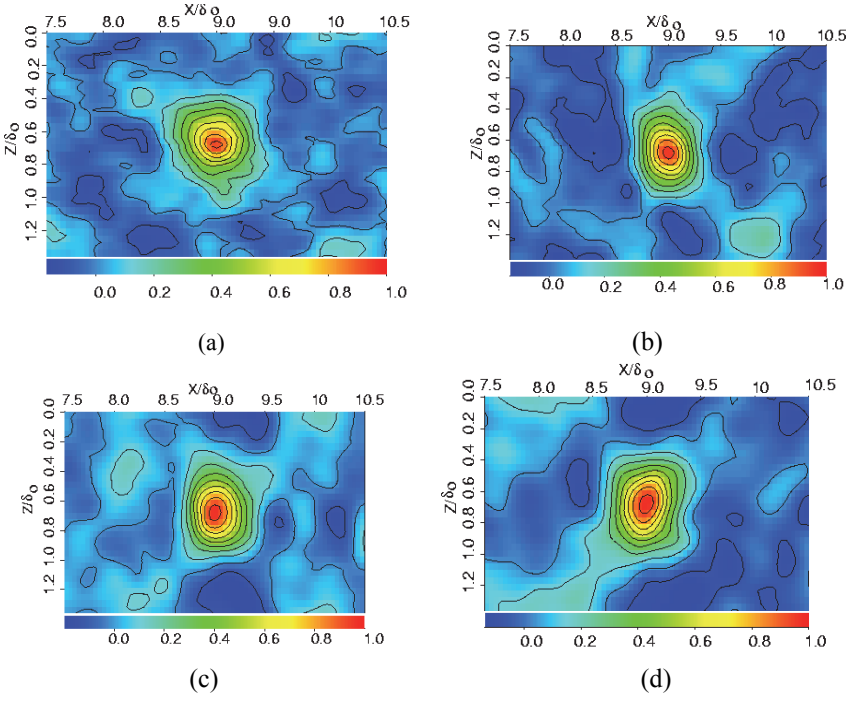

Figure 3: Spanwise correlation contours $R(w'(r)w'(r+\Delta r))$ in z-x plane at different vertical positions y/δ

behavior confirms the monotone increase of the turbulent length scale with normal distances from the wall. The decay approaching zero values clearly shows that the size of the domain in the spanwise direction suffices. Right adjacent to the wall the pronounced oscillations indicate the impact of the wall on the correlation behavior. These distributions can be used to assess whether the computational domain in the spanwise direction is sufficiently wide to accommodate the turbulence dynamics and hence the ability of using the recycling boundary condition in such direction.

The variations across the boundary layer of the mean density, static pressure, and temperature are shown in Fig. 5. Both the mean pressure p/p_∞ and total temperature T_o/T_∞ are constant in the inner layer of the boundary layer, but the total temperature increases slightly near the outer edge of the boundary layer. The mean density ρ/ρ_∞ increases across the boundary layer by nearly factor of 2.6 and the mean temperature T/T_∞ decreases by approximately a factor of 2.6 across the layer. The non-dimensional Van-Driest transformed velocity ($U^+_{VD} = U_{VD}/u_\tau$) is plotted

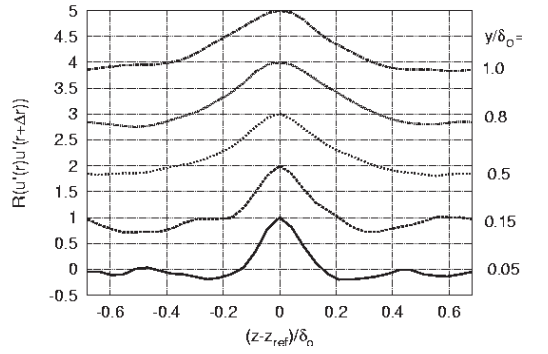

(a)

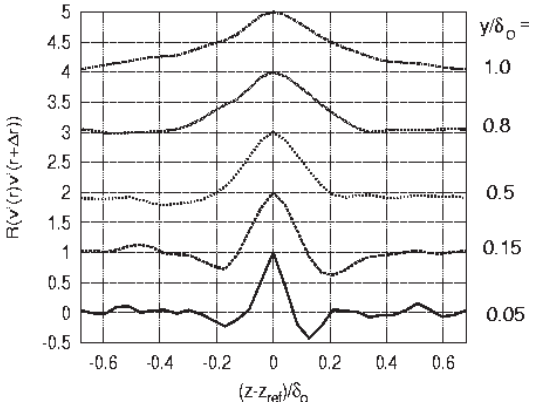

(b)

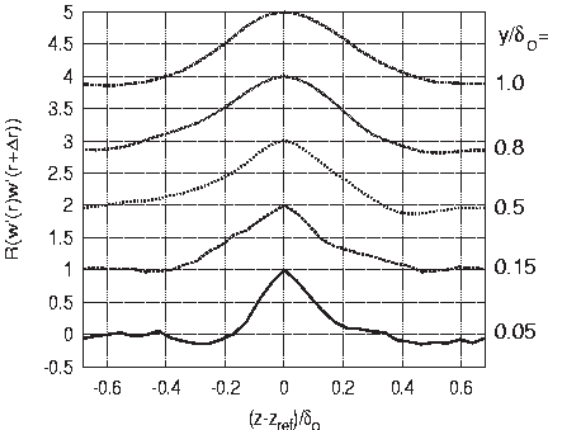

(c)

Figure 4: Autocorrelation-coefficient profiles in spanwise direction direction at different vertical positions y/δ. (a) $R(u'(r)u'(r+\Delta r))$ (b) $R(w1'(r)w'(r+\Delta r))$ (c) $R(v'(r)v'(r+\Delta r))$

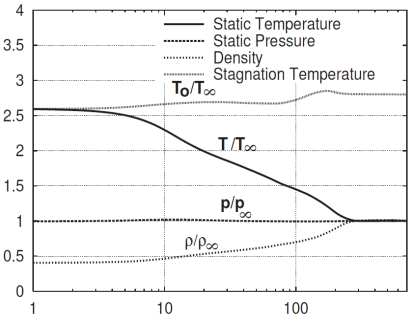

Figure 5: Variation of the mean thermodynamic variables: Total temperature, Static temperature, Static pressure and Density; across the boundary layer

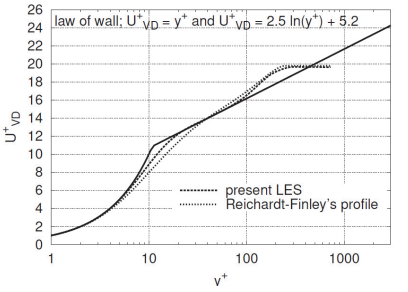

Figure 6: Van-Driest mean velocity (U^+_{VD}) distribution across the boundary layer compared with Reichard's profile with Finley's wake function. Solid lines represent sublayer and standard log law

in the wall units (y^+) in Fig. 6, where the Van-Driest transformed velocity can be computed as:

$$U_{VD}/U_\infty = \sin^{-1}(B \times U/U_\infty)/B$$

, with

$$B = \sqrt{0.5(\gamma-1) \times M_\infty^2 \times r/(1+0.5(\gamma-1) \times M_\infty^2 \times r)}.$$

On the plot the linear sub-layer relation ($U^+_{VD} = y^+$), the standard log-law ($U^+_{VD} = 2.5\ell n y^+ + 5.2$)
and the composite profile of Reichardt's inner layer and Finley's wake function given in Guarini, Moser, Shariff and Wray(2000) are included. The composite profile reads:

$$U^+_{VD} = \kappa^{-1}\ell n(\kappa y^+ + 1) + c_1(1 - e^{-(y^+/\eta_1)} - y^+ \times e^{-(b \times y^+)}/\eta_1) + \kappa^{-1}[(1+6\pi)(y/\delta)^2 - (1+4\pi)(y/\delta)^3],$$

where δ is the boundary layer thickness and the constants $c_1 = -\kappa^{-1}\ell n(\kappa) + c$, where $\kappa = 0.4$, $c = 4.7$, $\eta_1 = 11$ and b = 0.33. In the region $20 \leq y^+ \leq 80$, the simulation data fall on the log-law curve. The value of π for the time-averaged profile is $\pi = 0.25$as given in Guarini, Moser, Shariff and Wray(2000). The present LES results give good representation of U^+_{VD} throughout the boundary layer. This can be observed from the collapse with log-law and the composite profile of Reichardt's inner layer with Finley's wake function.

5.2 Expansion-compression ramp results

A large eddy simulation of spatially developing supersonic turbulent boundary layer past the expansion-compression ramp is performed. The spanwise extension of the $M_\infty = 2.9$ boundary layer, used to prescribe the inflow for the backward-facing step flow, is considered. The whole computational domain is subdivided into a set of 5 sub-domains. To ensure a proper balancing of the computational load between processing elements, each sub-domain contains the same number of grid points. The computation achieves a parallel efficiency of 98.4%. The grid, which is clustered in the expansion and compression corners, consists of $621\times113\times33$ cells in the x,y and z directions, respectively, resulting in a mesh of 2.32×10^6 grid points, see Fig. 7. The grid is stretched in y-direction with a spacing of $0.0028\delta_o$ near the wall and stretching factor of 1.05. The grid is smoothing concentrated in the streamwise direction at near of the corners. For more details of the present grid and that of Knight, Yan, Panaras and Zheltovodov(2003), see Tab. 1. For the present simulation, including the inflow generator, the time step is given as: $\Delta t \times a_o/\delta_o = 0.005$, where $a_o = \sqrt{\gamma RT_o}$ is the sound speed calculated at the stagnation temperature T_o. The time required for the freestream flow to traverse the computational domain can be computed as: $\Delta t_{domain} \times a_o/\delta_o = (L_u + L_d) \times a_o/(U_\infty \times \delta_o) = 13.3866$. This corresponds to 2677 calculation-time steps. The time averaging period is considered to be 3.9 flow times through the streamwise extent $(L_u + L_d)$.

Table 1: Details of grid: A comparison between the present LES () with total number of cells 2.32×10^6 and that of Knight, Yan, Panaras and Zheltovodov(2003) () with total number of cells 2.4×10^6

Case	$\Delta x^+_{\max}$ $\equiv \Delta x_{\max}/\delta_o$	$\Delta x^+_{\min}$ $\equiv \Delta x_{\min}/\delta_o$	$\Delta y^+_{\min}$ $\equiv \Delta y_{\min}/\delta_o$	Δz^+ $\equiv \Delta z/\delta_o$
Present	20 0.096	0.5 0.0028	0.5 0.0028	8.9 0.0425
Knight, Yan, Panaras and Zheltovodov(2003)	20.9 0.1	Not given Not given	1.67 0.008	7.1 0.034

The vortical structures near the wall are evidenced by λ_2- isocontours along the entire domain Jeong and Hussain(1995). The λ_2- definition is found to represent the topology and geometry of vortex cores correctly for the large variety of the considered flow. It corresponds to the pressure minimum in a plane vertical to the rotation axis; see Jeong and Hussain(1995). An overall impression of the intricacy

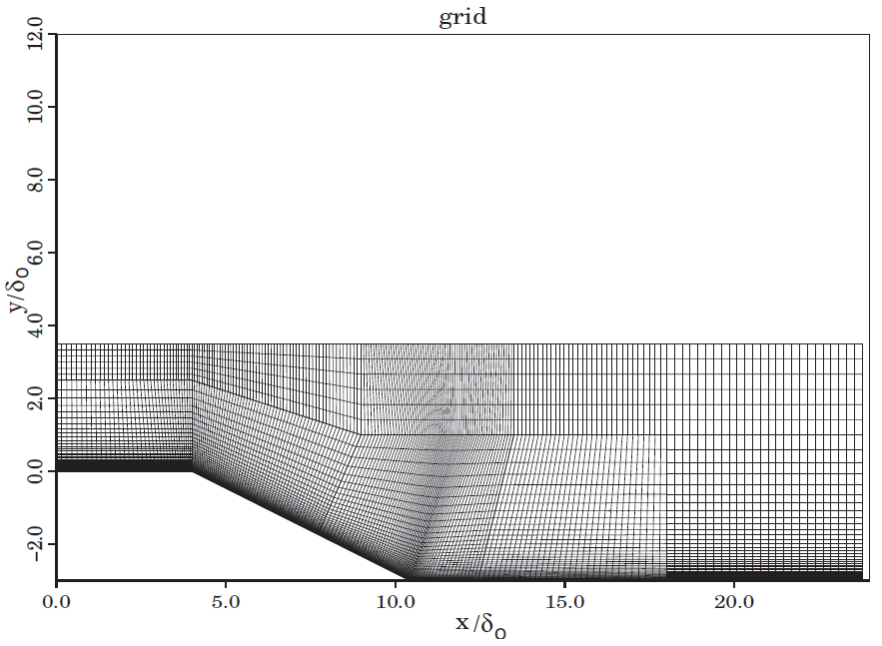

Figure 7: Grid used in the present LES of a supersonic turbulent flow near an expansion-compression ramp (an inclined 25-degrees backward-facing step).

of the flow field is given by the vorticity pattern, expansion waves and shock-wave shapes in Fig. 8. The fingerlike structure of eddies embedded in the boundary layer before the expansion can be clearly visible. After the expansion a strong lifting up and ejection from near wall to the outer layer of the boundary layer causes an elongation of eddies as noticed. A visualization of the instantaneous shock surface, which dissolves in the boundary layer, and the near-wall vorticity contours color coded by the local pressure is also observed. The fine scale structures after the shock indicate an increase in vorticity downstream of the compression-corner point due to the shock-boundary layer interaction. The increase of pressure after the shock enhances the sweeping of flow from outer layer to near the wall and hence reducing the inclination angle of vortices after the shock.

Flow visualization given by the instantaneous entropy contours is shown in Fig. 9. The figure clearly shows the large-scale bulges before the expansion corner and then subsequently elongation of bulges towards the outer layer of the boundary layer after the expansion. The instantaneous systems of expansion and compression waves near the expansion and compression zones, respectively, can be clearly seen.

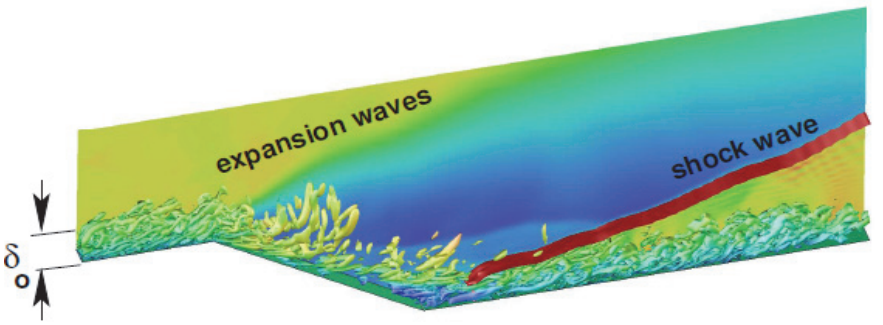

Figure 8: Visualization of the turbulent vortex structures in the boundary layer using λ_2-criteria. The expansion and the shock surfaces are included by iso-pressure contours.

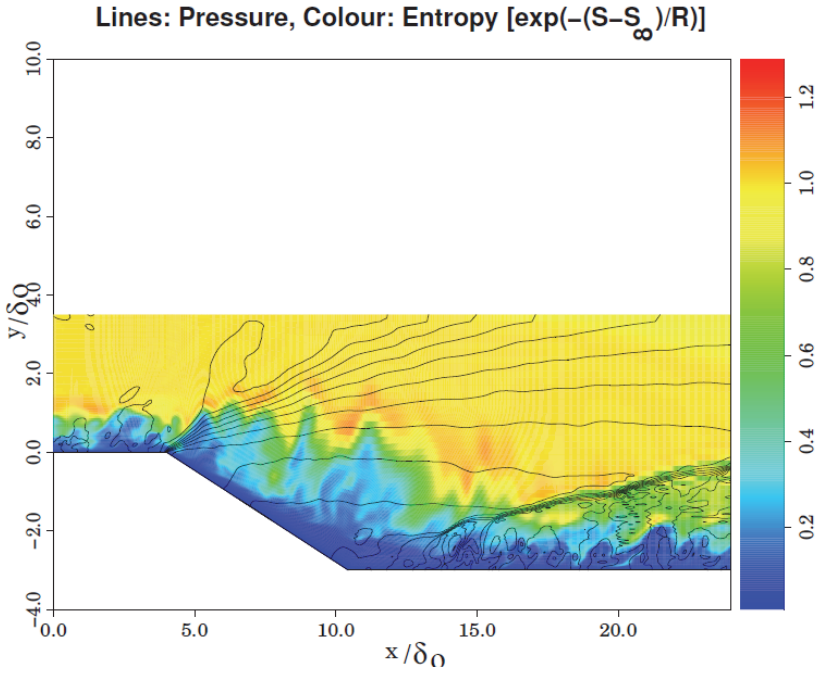

Figure 9: Instantaneous entropy contours

In the following, the mean quantities represent combined time and spanwise averages. The dimensionless mean streamwise velocity contours U/a_o are given in Fig. 10. The time-averaged compression waves eventually coalesce together to form an inclined shock wave. The dissolvation of the shock roots is clearly observed due to the near wall subsonic region in the boundary layer. The separation bubble can be also noticed in the compression corner region, due to the generated compression waves. It is evident that a high velocity gradient downstream of the interaction region is produced.

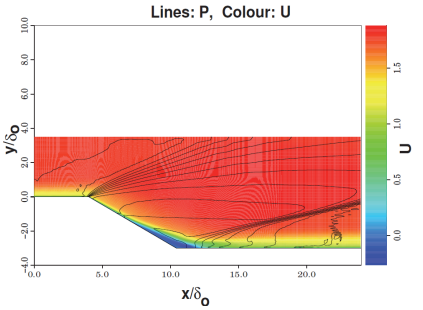

Figure 10: Time-averaged streamwise velocity contours

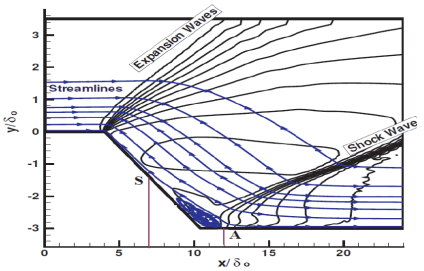

Figure 11: Mean streamlines and static pressure contours (**S** denotes separation points and **A** is the reattachment point)

The computed flow-field structure is shown in Fig. 11 which displays the mean static pressure and streamlines patterns (S is the separation point and A the attachment point). The flow expands around the expansion corner and recompresses at the second compression one. The shock-wave turbulent boundary-layer interaction (SWTBLI) produced by the second corner is sufficiently strong to separate the boundary layer to form a separation bubble as evident in Fig. 11.

The mean streamwise velocity profiles at $x/\delta_o = 2$ (i.e., over the flat surface upstream of the expansion point which is located at $x/\delta_o = 4$) are compared in Fig. 12, where x is considered from the inflow along the inflow freestream velocity. The quality of the developed inflow boundary condition is clearly indicated by the agreement with the experiment of Zheltovodov, Trofimov, Schuelein and Yakovlev (1990) not only right adjacent to the surface but also at the edge of the boundary layer. Further comparison between the present LES and that of Knight, Yan, Panaras and Zheltovodov(2003) at $x/\delta_o = 6$ is given in Fig. 13.

The elongation of vortex structure after the expansion which causes strong ejection and traversing of momentum from near the wall to the outer layer is seen in the present LES. This can be visibly seen from the reduction of velocity gradi-

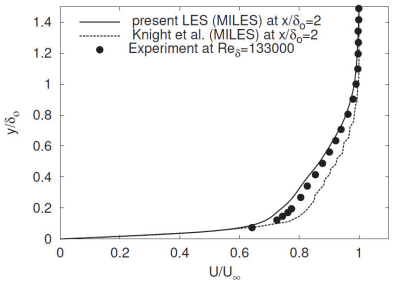

Figure 12: Mean streamwise velocity profile at $x/\delta_o = 2$ in comparison to experimental data of Zheltovodov, Trofimov, Schuelein and Yakovlev(1990) and LES of Knight, Yan, Panaras and Zheltovodov(2003)

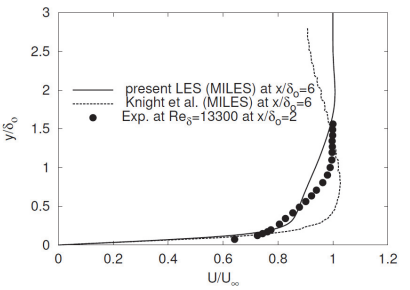

Figure 13: Mean streamwise velocity profile at $x/\delta_o = 6$ in comparison to experimental data of Zheltovodov, Trofimov, Schuelein and Yakovlev(1990) and LES of Knight, Yan, Panaras and Zheltovodov(2003)

ent near the wall. It must be explained here that the mean streamwise velocity approaches its inflow freestream velocity U_∞ above the expansion fan, nearly at $y/\delta_o = 2$ as observed in the present LES. No pronounced prediction of this approaching from the results of Knight, Yan, Panaras and Zheltovodov(2003) was obtained. The concavely curvature of the streamlines before separation bubble is responsible for the reduction of velocity gradient in the outer layer of the boundary layer. A reversed phenomenon is noticed from the data of Knight, Yan, Panaras and Zheltovodov(2003), see Fig. 13.

The non-dimensional wall-pressure (P/P_∞) and wall skin-friction coefficient ($c_f = \sigma_w/(0.5\rho_\infty U_\infty^2)$) distributions along with the computation of Knight, Yan, Panaras and Zheltovodov(2003) and the experiments of Zheltovodov, Trofimov, Filippova and Yakovlev(1990) and Zheltovodov, Trofimov, Schuelein and Yakovlev(1990) are provided in Figs. 14 and 15, respectively. The profiles display a pressure plateau on the compression face generated by the separation bubble. The experimental data ($Re_\delta = 4.07 \times 10^4$) shows close agreements with all numerical data. However, close distributions of the experimental data and the present LES compared with that of Knight, Yan, Panaras and Zheltovodov(2003) are noticed. The present LES indicates, unlike the numerical solution from Knight, Yan, Panaras and Zheltovodov(2003), a satisfactory agreement with the measured skin friction after reattachment. No measurements are considered in the separation bubble as mentioned in Knight, Yan, Panaras and Zheltovodov(2003). The skin friction coefficient increases rapidly downstream of the reattachment due to the compression effect which reduces the inclination angles of eddies and hence a reduction of the

boundary layer thickness so that the velocity gradient increases near the wall. It is concluded from this figure that the present LES results are juxtaposed with the experimental data.

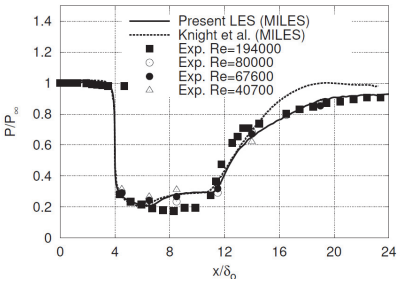

Figure 14: Surface pressure distribution in comparison to experimental data of Zheltovodov, Trofimov, Filippova and Yakovlev(1990) and Zheltovodov, Trofimov, Schuelein and Yakovlev(1990) and LES-computation of Knight, Yan, Panaras and Zheltovodov(2003)

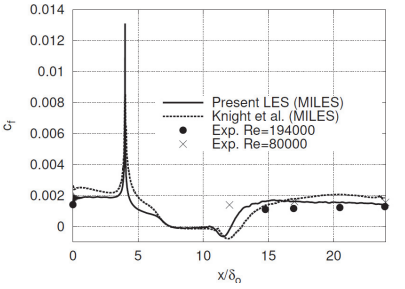

Figure 15: Skin-friction coefficient distribution in comparison to experimental data of Zheltovodov, Trofimov, Filippova and Yakovlev(1990) and Zheltovodov, Trofimov, Schuelein and Yakovlev(1990) and LES-computation of Knight, Yan, Panaras and Zheltovodov(2003)

The streamwise velocity profiles, transformed according to van Driest at several streamwise locations (x/δ_o =2, 4, 6, 7, 11, 15, 18, 22 and 23) compared with the law-of-the wall profile are shown in Fig. 16. It is clear that the upper profile (at x/δ_o =2) is fully turbulent equilibrium boundary layer profile. Within the region of mean-flow separation wall scaling has no meaning and profiles are not shown. After of the compression-corner point all profiles show a characteristic 'dip' below the law-of-the-wall solution, which decays for the downstream located profiles. A similar behavior was found by El-Askary, Schröder and Meinke(2003) in the compression ramp simulation. This deviation below the logarithmic law suggests an increase in the dissipation length scale over the equilibrium value. At station x/δ_o =4 one notices a large deviation from the law of the wall due the strong turning past the expansion corner which leads to an increase of shear velocity in the boundary layer of this zone. Before approaching the compression corner the flow goes to concavely turn past the generated separation bubble at the corner and hence a reduction of the shear velocity and consequently increases the value of U^+_{VD}.

The dimensionless mean-velocity profiles spanning the expansion as well as the shock boundary layer interaction regions are shown in Fig. 17. These profiles are

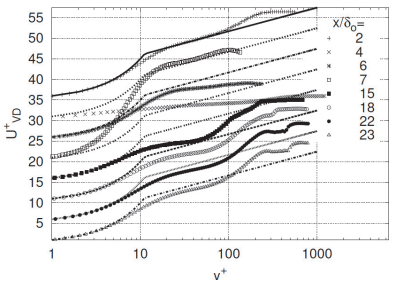

Figure 16: Van-Driest transformed velocity profiles U_{VD}^{+}

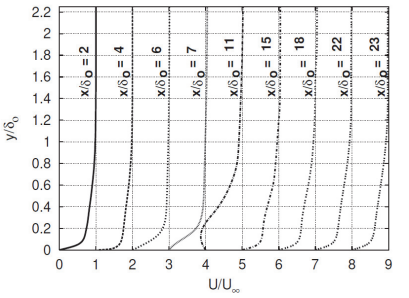

Figure 17: Streamwise velocity profiles at several streamwise locations vs. y^{+} and standard law of the wall at several streamwise locations

identified by its local streamwise position. The first profile (at $x/\delta_o = 2$) is that of an equilibrium turbulent profile for velocity, as previously discussed. The profile at separation ($x/\delta_o = 11$) is identical to the first profile, except that it is retarded below $y/\delta_o = 0.24$. However, the strong energy transfer from the near wall to the outer layer can be observed from the temperature profile at this station, see Fig. 18. Profiles after reattachment show a gradual recovery, such that the last station profile (at x/δ_o =23) is not obviously different from an equilibrium turbulent boundary-layer shape. The location of the shock generated by the compression corner appears as a kink in temperature profiles as x/δ_o =15, 18, 22 and 23. The developing of the time-averaged density profiles passing the expansion-compression corners are also presented in Fig. 19. Due to expansion waves, a reduction in density can be observed near the wall at stations x/δ_o =6 and 7. By approaching near and after compression corner, density starts to increase and all kinks in the last four density profiles still display the induced shock wave.

There is rarely available experimental documented-data for the turbulent stresses in supersonic boundary layer. For the author knowledge, the influence of this complex geometry on turbulence behavior has not been widely presented. The reason for this scarcity of measurements and their generally poor quality is simple: the measurement of turbulence quantities in supersonic boundary layers is exceedingly difficult, with the level of difficulty increasing with flow complexity as given in the present studied case. The turbulent-Reynolds stresses and turbulence kinetic energy produced by developing supersonic flow past an expansion-compression ramp is numerically given in Figs. 20-23.

The effect of the expansion-compression corner can be directly observed. A re-

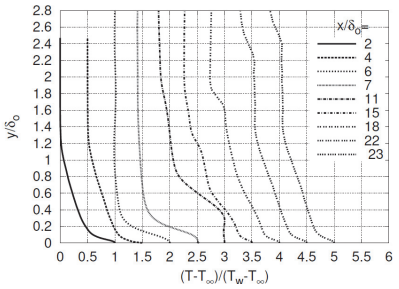

Figure 18: Dimensionless temperature profiles at several streamwise locations

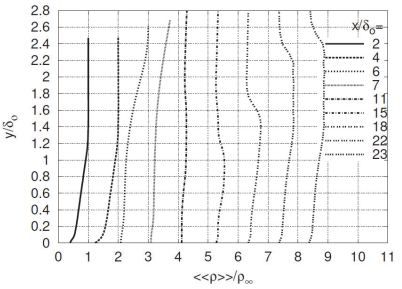

Figure 19: Dimensionless density profiles at several streamwise locations

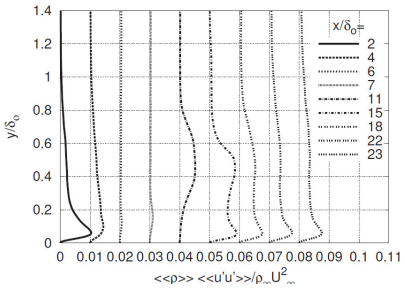

Figure 20: Dimensionless turbulent-Reynolds stress in streamwise direction at several streamwise locations

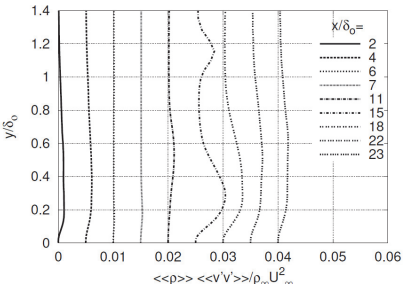

Figure 21: Dimensionless turbulent-Reynolds stress in vertical direction at several streamwise locations

duction of all turbulence stresses near the expansion corner, due to the convexity of the streamlines near it, while an enhancement of turbulence due to the concavity near the compression corner. Due to the energy transfer to the outer layer, a shift of the peaks is seen after the expansion ($x/\delta_o = 6$, 7 and 11). Downstream the shock, the peak value occurs closer to the wall than upstream and a certain plateau develops before the decay sets (x/δ_o =15, 18, 22 and 23). Traveling after the compression corner to the end of the domain, the profiles develop to approach equilibrium distributions. Because the appearance of the shock, which interacts with the boundary layer at the corner, this will lead as discussed previously to the distortion of the turbulent vortices in the boundary layer, and as such will enhance the turbulent motion in the boundary layer. The increase of the turbulent kinetic energy is also emphasized by the development of the time-averaged kinetic energy $<< k >>= 0.5(\overline{u'u'} + \overline{v'v'} + \overline{w'w'})$ shown in Fig. 23. This is also indicated by the dip below the log law shown in Fig. 16 at stations x/δ_o =15, 18, 22 and it causes

destabilizing effects on the boundary layer. At station x/δ_o =11, i.e., in the separation region strong mixing and dissolvation of the shock wave in the outer part of the boundary layer. This leads to activation and shifting of turbulence behavior far from the wall. The second peaks observed in $\overline{v'v'}$ and « k » at approximately y/δ_o =1.18 are due to the intersection of the shock at this location.

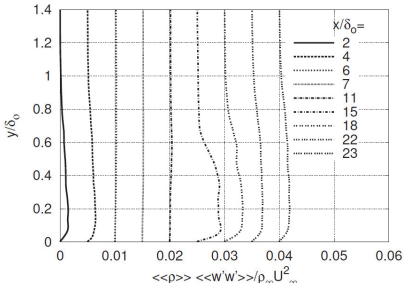

Figure 22: Dimensionless Turbulent-Reynolds stress in spanwise direction at several streamwise locations

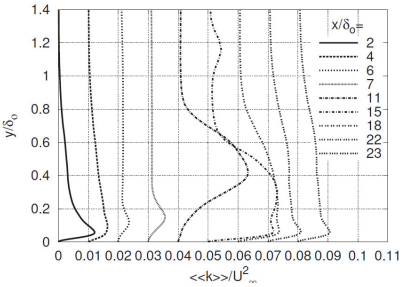

Figure 23: Dimensionless time-averaged turbulent kinetic energy at several streamwise locations

As a main indicator for the compressibility effects, the turbulent Mach number is often used, which is defined as: $M_t = \sqrt{\overline{u'u'} + \overline{v'v'} + \overline{w'w'}}/\bar{a}$, where $\bar{a}$ is the local mean speed of sound; $\bar{a} = \sqrt{\gamma R\bar{T}}$. Figure 24 shows distributions of the turbulent Mach number at the given different streamwise positions. According to Spina, Smits snd Robinson(1994) the turbulence is only weakly affected by compressibility provided $M_t \leq 0.3$ at station x/δ_o =2 which is in fact the case in this computation of the inflow generator. This supports the validity of Morkovin's hypothesis [Bradshaw(1977)] used in the present work in which the total temperature fluctuation is neglected compared with the static temperature fluctuation. However, the convection of turbulence energy from near the wall to outer layer is responsible for the decrease of turbulent Mach number after expansion. The turbulent Mach number assumes a maximum value of about 0.47 in the interaction region of the compression zone, rising from about 0.3 at x/δ_o =2 on the upstream flat surface.

6 Conclusion

Large-eddy simulation of supersonic turbulent flow past an expansion-compression ramp of 25 degrees was performed. The rescaling method to generate a turbulent flow distribution was extended to compressible flow through a new formulation of the temperature profile. An inner- and outer-layer temperature rescaling were derived to generate suitable inflow condition for supersonic boundary layer at Mach

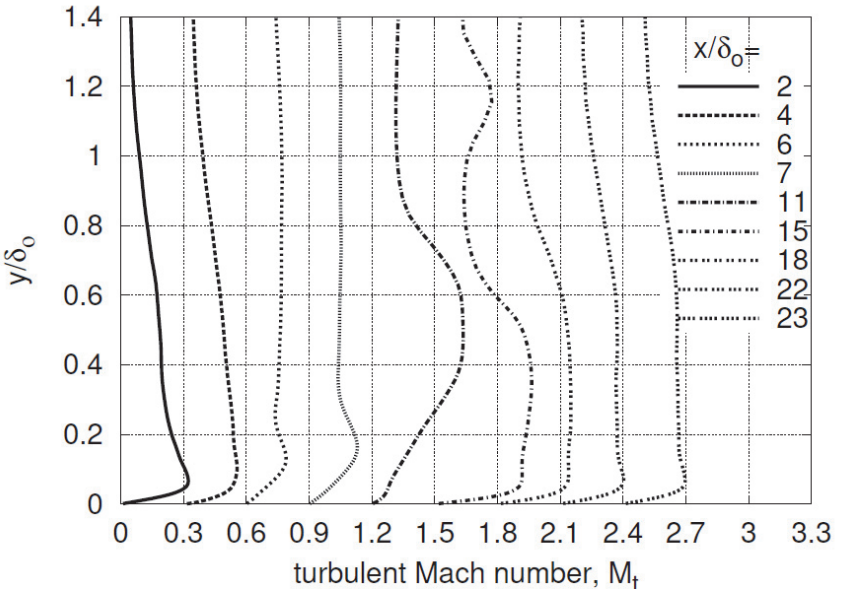

Figure 24: Turbulent Mach number at several streamwise locations

number of 2.9. The supersonic boundary layer simulation was used as an inflow generator to the expansion-compression ramp to examine the realisticity and quality of the inflow generator.

Analysis of the undisturbed turbulent boundary layer (inflow generator) was performed and statistics were generally in good agreement with Reichardt's inner layer and Finley's wake function in the literature. The author was also able to show that, through use of recycling/rescaling method with its extension to compressible boundary layer, no non-physical correlations were observed in the undisturbed boundary layer which could be imparted to the expansion-compression corner flow simulation.

An overall agreement with experimental and numerical data for the expansion-compression configuration including surface pressure, skin friction, and velocity profiles was convincing. Separation bubble near the compression corner was predicted through streamlines contours as well as the wall skin-friction coefficient.

Turbulent stresses, which are rarely available in the experimental documentations, were also presented to show the enhancement of turbulence energy after expansion and the recovery development after reattachment. It has to be kept in mind that the considered simulation was at lower Reynolds number than that of the exper-

imental work. For industrial flows the Reynolds number is typically a factor of 10^3 higher and according near-wall resolution is computationally not feasible with present LES. For this reason, it is recommended to extend the simulation to hybrid LES/RANS or Detached Eddy Simulation (DES) ansatz plus wall functions to satisfy sufficient resolution. Attention has to be also directed to the integration scheme that enables varying time steps without reducing the computation efficiency.

References

Adams, N. A. (1997): Direct numerical simulation of turbulent supersonic boundary layer flow. *Advances in DNS/LES, Proceedings of the First AFOSR International Conference on DNS/LES*, Greyden press Columbus, pp. 29–40.

Adams, N. A. (2000): Direct simulation of the turbulent boundary layer along a compression ramp at M=3 and $Re_\theta = 1685$. *J. Fluid Mechanics,* vol. 420, pp. 47–83.

Boris, J. P.; Grinstein, F. F.; Oran, E. S.; Kolbe, R. L. (1992): New insights into large eddy simulation. *Fluid Dynamics Research*, vol. 10, pp. 199-228.

Bradshaw, P. (1977): Compressible turbulent shear layers. *Ann. Rev. Fluid Mechanics*, vol. 9, pp. 33-54.

El-Askary, W. A.; Meinke, M.; Schröder, W. (2001): Towards the numerical analysis of trailing-edge noise. *DGLR-JT*, 2001-176.

El-Askary, W. A.; Schröder, W.; Meinke, M. (2003): LES of compressible wall-bounded flows. *AIAA Paper* 2003-3554, Orlando, Florida.

El-Askary, W. A. (2003): Large eddy simulation of subsonic and supersonic wall-bounded flows. Abhandlung aus dem Aerodynamischen Institut der RWTH Aachen, Heft 34, Institute of Aerodynamics Aachen University, Editor: Prof. Dr. W. Schröder, Aachen, Germany, pp. 12–27.

El-Askary, W. A.(2009): Turbulent boundary layer structure of flow over a smooth-curved ramp. *Journal of Computers & Fluids,* vol. 38, no. 9, pp. 1718-1730.

Favre, A. (1965): Equations des gaz turbulents compressibles. *Journal de Mecanique*, 4, pp. 361-390.

Fureby, C.; Grinstein, F. F. (2002): Large eddy simulation of high-Reynolds-number free and wall-bounded flows. *J. of Computational Physics*, vol. 81, pp. 68-97.

Grinstein, F. F.; Fureby, C. (2002): Recent progress on MILES for high Reynolds number flows. *J. Fluids Eng.*, vol. 124, pp. 848–861.

Guarini, S. E.; Moser, R. D.; Shariff, K.; Wray A. (2000): Direct numerical simulation of a supersonic turbulent boundary layer at Mach 2.5. *J. Fluid Mechanics*,

vol. 414, pp. 1-33.

Guo, X.; Schröder, W.; Meinke, M. (2006): Large eddy Simulations of Film Cooling Flows. *J. of Computers & Fluids*, vol. 35, pp. 587-606.

Jeong, J.; Hussain, F. (1995): On the identification of a vortex. *J. Fluid Mechanics*, vol. 285, pp. 69-94.

Knight, D. D.; Degrez, G. (1998): Hypersonic experimental and computational capability, improvement and validation. *Technical Report AGARDograph*, No. 319, AGARD, Neuilly sur Seine, France.

Knight, D.; Zhou, G.; Okong'o, N; Shukla, V. (1998): Compressible large eddy simulation using unstructured grid. *AIAA Paper* 98-0535.

Knight, D.; Yan, H.; Panaras, A. G.; Zheltovodov, A. (2003): Advances in CFD prediction of shock wave turbulent boundary layer interactions. *Progress in Aerospace Sciences*, vol. 39, pp. 121-184.

Lund, T. S.; Wu, X.; Squires, D. (1998): Generation of turbulent inflow data for spatially-developing boundary layer simulations. *J. of Computational Physics,* vol. 140, pp. 233-258.

Meinke, M.; Schröder, W.; Krause, E.; Rister, T. (2002): A comparison of second- and sixth-order methods for large-eddy simulations. *J. Comput. Fluids,* vol. 31, pp. 695–718.

Poinsot, T. J.; Lele, S. K. (1992): Boundary conditions for direct simulations of compressible viscous flows. *J. of Computational Physics,* vol. 101, pp. 104-129.

Renze, P; Schröder, W.; Meinke, M. (2008): Large-eddy simulation of film cooling flows with variable density jets. *J. of Flow Turbulence Combust*, vol. 80, pp. 119–132.

Rizzetta, D. P.; Visbal, M. R.; Gaitonde, D. (2001): Large-eddy simulation of supersonic compression-ramp flow by high-order method. *AIAA J.*, vol. 39, pp. 2283–2292.

Roache, P. J. (1976): *Computational Fluid Dynamics*. Hermosa Publ., Albuquerque, New Mexico.

Sagaut, P.; Garnier, E.; Tromeur, E.; Larcheveque, L.; Labourasse, E. (2004): Turbulent inflow conditions for large-eddy simulation of compressible wall-bounded flows. *AIAA J.*, vol. 42, pp. 469–477.

Schröder, W.; Meinke, M.; Ewert, R.; El-Askary, W. A. (2001): Turbulent flow around a sharp trailing edge. *Direct and Large-Eddy Simulation IV*, Kluwer Academic, Norwell, MA, pp. 353–363.

Spalart, P. R. (1988): Direct simulation of a turbulent boundary layer up to $Re_\theta =$

1410. *J. Fluid Mechanics*, vol. 187, pp. 61-98.

Spina, E. F.; Smits, A. J.; Robinson, S. K. (1994): The physics of supersonic turbulent boundary layers. *Ann. Rev. Fluid Mechanics*, vol. 26, pp. 287-319.

Urbin, G.; Knight, D.; Zheltovodov, A. (2000): Large eddy simulation of a supersonic compression corner. *AIAA Paper* 2000-0398.

Urbin, G.; Knight, D. (2001): Large eddy simulation of a supersonic boundary layer using an unstructured grid. *AIAA J.*, vol. 39, no. 7, pp. 1288–1295.

Walz, A. (1969): *Boundary layers of flow and temperature*. MIT Press.

Xiao, X.; Edwards, J. R.; Hassan, H. A. (2003): Inflow boundary conditions for hybrid large eddy/Reynolds averaged Navier-Stokes simulations. *AIAA J.*, vol. 41, pp. 1481–1489.

Xu, S.; Martin, M. P.(2004): Assessment of inflow boundary conditions for compressible turbulent boundary layers. *J. Phys. Fluids*, vol. 16, pp. 2623–2639.

Yan, Y; Urbin, G.; Knight, D.; Zheltovodov, A. (2000): Compressible large eddy simulation using unstructured grid: supersonic boundary layer and compression ramps. 10th International Conference on Methods of Aero-physical Research, July 9-16, Novosibirsk, Russia.

Zheltovodov, A.; Trofimov, V.; Filippova, E.; Yakovlev, N. (1990): Influence of turbulence change on the heat exchange under conditions of supersonic separated flows. In Abstracts: IUTAM Symposium on Separated Flows and Jets, pp. 273-274, USSR Academy of Sciences, Siberian Division, Novosibirsk.

Zheltovodov, A.; Trofimov, V.; Schuelein, E.; Yakovlev, N. (1990): An experimental documentation of supersonic turbulent flows in the vicinity of forward- and backward-facing ramps. Institute of Theoretical and Applied Mechanics, Rep. No. 2030, USSR Academy of Sciences.

Zheltovodov, A.; Schuelein, E.; Horstman, C. (1993): Development of separation in the region of interaction of shock wave with turbulent boundary layer disturbed by expansion. *Journal of Applied Mechanics and Technical Physics*, vol. 3, pp. 58-68 (in Russian).

Zheltovodov, A. (2006): Some advances in research of shock wave turbulent boundary layer interactions. *AIAA Paper* 2006-0496.